

# Investigation and Modeling of the Electrical Bias Stress in Electrolyte-Gated Organic Transistors

Matteo Segantini, Alberto Ballesio,\* Gianluca Palmara, Pietro Zaccagnini, Francesca Frascella, Giovanna Garzone, Simone Luigi Marasso, Matteo Cocuzza, and Matteo Parmeggiani

Electrolyte-gated organic transistors (EGOTs) are emerging as an important tool in advanced biosensing applications. However, their widespread exploitation is still limited by their poor operational stability. In order to understand the causes of this unreliability, the proposed study focuses on the influence of electrical bias stress (EBS) on EGOTs operating in aqueous electrolytes. Poly(3-hexylthiophene) (P3HT)- and poly[3-(5-carboxypentyl)thiophene] (P3CPT)-based transistors are studied under the application of a bias in the continuous and pulse mode. Combining electrical and spectroscopic characterizations, it is possible to ascribe the performance variation of P3HT devices to backbone rearrangements induced by side chain oxidation, hydration, and interfacial electrochemical doping at the semiconductor/electrolyte interface, while the presence of polar side chains in P3CPT enhances the oxidative degradation of the polymer throughout the bulk of the film. The charge-trapping model based on a stretched exponential is commonly exploited for the description of EBS in solid dielectric organic field-effect transistors (OFETs). The same model is here applied to fit liquid dielectric EGOT behavior. The extracted material parameters are in good agreement with those found in the literature for P3HT-based OFETs. Finally, a novel improvement of the model is proposed to allow reproducing P3CPT data by accounting for its different degradation process.

is coupled with the gate electrode via an electrolyte. The application of a bias to a polarizable gate electrode may either induce the formation of two electrical double layers or allow the intercalations of ions in the OSC film. In the first case, the transistors are operating in the field-effect mode and they are called electrolyte-gated organic field-effect transistors (EGOFETs), while in the second case, an electrochemical doping occurs and the devices are named organic electrochemical transistors (OECTs). EGOTs can operate with voltages below 1 V and are extremely sensitive to any change that occurs either on the gate electrode or on the OSC. For this reason, these devices are exploited in biosensing applications for the detection of specific binding events occurring at the gate surface, which is functionalized to match the targeted analyte. Indeed, EGOTs can be used as biosensors to detect low concentrations of relevant biomolecules (proteins,<sup>[1–3]</sup> nucleic acids,<sup>[4,5]</sup> drugs<sup>[6–8]</sup>), but the manufacturing of these devices for

## 1. Introduction

In the last decade, there has been a growing interest about the exploitation of electrolyte-gated organic transistors (EGOTs) as a new class of biosensors. These devices are transistors whose active material is an organic semiconductor (OSC) that

scale production and commercial applications is still far to be achieved. In fact, one of the main disadvantages of EGOTs is their poor operational stability, whose origins are still under investigation.<sup>[9–11]</sup>

Several works in the literature concerning organic transistors address the instability related to the electrical bias stress (EBS), but most of the proposed models deal with solid-state organic field-effect transistor (OFET).<sup>[12,13]</sup> For this kind of devices, the EBS is responsible for mobile charges trapping either in the OSC material, or in the insulating dielectric, or at the OSC/dielectric interface. This mechanism is usually related to high-voltage-induced water electrolysis phenomena affecting adsorbed adventitious water molecules present on the oxide surface.<sup>[12,14]</sup> The EBS in EGOTs should be ascribed to different causes since the low operating voltages prevent any water electrolysis to occur. In addition to this, the different nature of the dielectric material avoids any charge accumulation in the dielectric, being the ions in the electrolyte free to move. Concerning the operational stability of EGOTs, only a limited number of works are found in the literature addressing the issue. For instance, Blasi et al. investigated the long-term stability of EGOFETs based on poly(3-hexylthiophene) (P3HT), showing that the maximum current drift over time could be modeled with a biexponential function, in which two processes with different timescales occur.<sup>[15]</sup>

M. Segantini, A. Ballesio, G. Palmara, P. Zaccagnini, F. Frascella, G. Garzone, S. L. Marasso, M. Cocuzza, M. Parmeggiani  
 Department of Applied Science and Technology (DISAT)  
 Politecnico di Torino  
 Corso Duca degli Abruzzi 24, Torino 10129, Italy  
 E-mail: alberto.ballesio@polito.it  
 S. L. Marasso, M. Cocuzza  
 CNR-IMEM  
 Parco Area delle Scienze, 37a, Parma 43124, Italy

 The ORCID identification number(s) for the author(s) of this article can be found under <https://doi.org/10.1002/aelm.202101332>.

© 2022 The Authors. Advanced Electronic Materials published by Wiley-VCH GmbH. This is an open access article under the terms of the Creative Commons Attribution-NonCommercial-NoDerivs License, which permits use and distribution in any medium, provided the original work is properly cited, the use is non-commercial and no modifications or adaptations are made.

DOI: 10.1002/aelm.202101332

A similar work was performed by Picca et al., who recorded a transfer characteristic curve every 30 min on a P3HT-based EGOFET and demonstrated that the signal stabilization over time was attributable to the polymer surface modification given to the exposure to water.<sup>[16]</sup> In another work, the instabilities of EGOFETs were related to a decrease of the charge mobility due to the widening of trapping states according to the Vissenberg–Matters model.<sup>[17]</sup> Kim et al. investigated instead how the crystallinity of the organic semiconductor influences the long-term stability of OECTs.<sup>[18]</sup> However, while these works try to model and assess the causes of the EGOT instabilities, they lack a systematic study of the effects of the application of an EBS, which is a fundamental aspect to be taken into account in specific applications such as real-time biosensing, where the measurement protocol may introduce an additional and unwanted signal variation.<sup>[19,20]</sup>

In this work is therefore reported a study on the stability of EGOTs based on two commercial p-type semiconductive polymers, with particular focus on the impact of the EBS on the device performances. For this study, two polymers are compared, namely P3HT and poly[3-(5-carboxypentyl)thiophene-2,5-diyl] (P3CPT). These two polymers are widely used in literature and they have been extensively characterized in terms of operations mode: while P3HT-based transistors work in the field-effect mode (i.e., EGOFETs), the current modulation in P3CPT occurs through electrochemical doping (i.e., OECTs).<sup>[21–23]</sup> Despite their different operation modes, the chemical structure of the two polymer differs only in the terminal group of their side chains, P3HT presenting a methyl group, while P3CPT expose a carboxylic moiety. Thus, they are used in this work as benchmark polymers to compare the EBS impact in the two operating regimes.

Microfabrication techniques were exploited to manufacture multiple devices (three) on the same chip for a redundant analysis. A microfluidic platform hosting the chip and the gate electrode was specifically designed to conduct this study, inspired by our previously proposed concept of a portable sensing card.<sup>[24]</sup>

Output and transfer characteristics, and cyclic voltammetry (CV) measurements have been performed on the two polymers in order to provide a complete characterization of the system under analysis.

Two distinct protocols were exploited for the application of the EBS: the continuous mode (CM) and the pulse transfer mode (PTM) protocols. In the CM, the channel and gate potentials ( $V_{DS}$  and  $V_{GS}$ , respectively) were constantly set to a fixed value, while in PTM, a linear scan of  $V_{GS}$  and a fixed  $V_{DS}$  were repeatedly applied through short pulses. A more detailed description of these protocols will be provided later on in the text.

It was demonstrated that the EBS in the CM causes a worsening of the performances over long periods, which is more evident and detrimental for P3CPT rather than P3HT. This result was attributed to an EBS-enhanced oxidative doping of P3CPT inducing an increase of disorder in the thin film, which was further confirmed through Raman spectroscopy characterizations. X-ray photoelectron spectroscopy (XPS) analysis further confirmed this result. Moreover, it also allowed revealing a partial oxidation of P3HT most superficial layer which was not detected by Raman analysis. The P3HT interfacial layer

interested by this oxidation is the same region involved in the field-effect accumulation of charge carriers. This degradation can therefore explain EGOFETs' long-term performance losses.

The short-term drift was investigated in the transfer pulse mode (TPM) and a mathematical model based on a stretched exponential function was proposed to describe the time evolution of transistors' characteristics in this regime. The results suggested two different sources of instability in the two polymers. In particular, a nonreversible oxidative degradation mechanism enabled by the presence of carboxyl-terminated side chains was responsible for the instability in P3CPT, while the drift of the output signal for P3HT could be interpreted in terms of a reversible backbone rearrangement at the solid/liquid interface inducing an undesired electrochemical doping of the most superficial layers.

These results shed light on the effective nature of EGOT volatility, therefore paving the way for a better design and managing of biosensors with long-term operational stability. Moreover, the proposed portable platform, composed by an integrated microfluidic device with an array of EGOTs, represents a perfect engineering and manufacturing implementation toward large-scale production, therefore enabling new opportunities in terms of applications for these devices.

## 2. Experimental Section

### 2.1. Microfluidic Platform

The microfluidic platform was designed to easily integrate the chip hosting the array of devices with the gold gate electrode and to allow a continuous flow of the electrolyte provided by an external pump (Figure 1).

The microfluidic chamber was obtained through replica molding technique, casting polydimethylsiloxane (PDMS) (Sylgard 184, with a 10:1 mixing ratio between the elastomer and the curing agent) into a 3D-printed master (Objet30 by Stratasys). The chamber presented two equal rectangular openings, one facing the gate electrode and the other one facing the interdigitated electrodes of the sensors. These windows defined the amount of exposed gate area, which was 9 mm<sup>2</sup> (4.5 mm × 2 mm) and ensured the electrolytic coupling between the devices and the gate electrode. The total volume of the chamber was equal to 50  $\mu$ L, with additional 30  $\mu$ L of the inlet and outlet channels.

To ensure the sealing of the PDMS channels, two polymethyl methacrylate holders were machined by exploiting a CO<sub>2</sub> laser cutting system (LaserScriber, Microla Optoelectronics Srl) to define the geometry and to pattern the housings for the chip and the gate electrode.

The proposed design of the microfluidic platform allowed characterizing the stability over time of the devices working in contact with an electrolyte under highly repeatable conditions. This was extremely useful since the results obtained with this structure might be exploited as calibration curves for the future application of EGOTs as biosensors. Moreover, a continuous flow of phosphate buffered saline (PBS) buffer into the chamber avoided changes of saline concentration of the solution due to liquid evaporation (the longest experiments lasted more than 16 h).

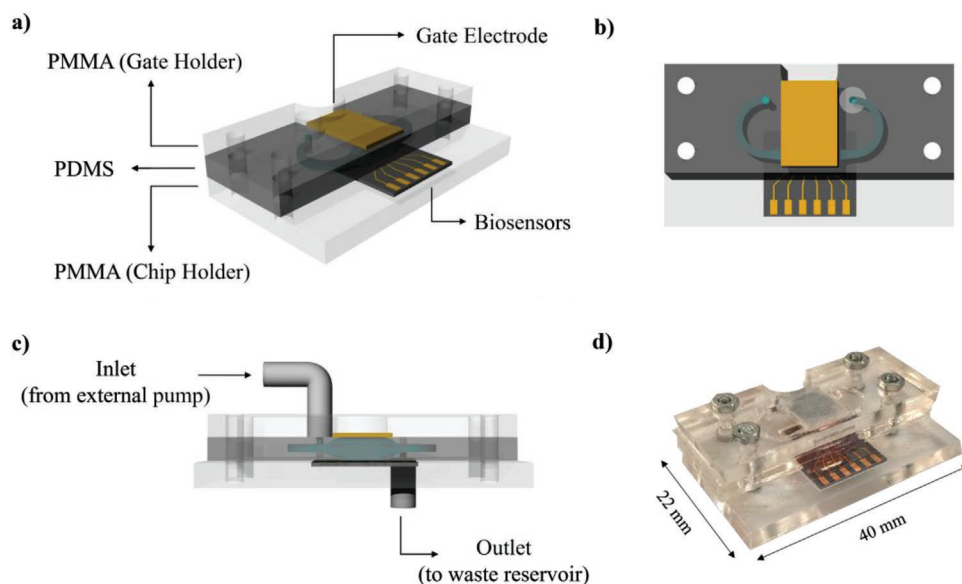


**Figure 1.** CAD representation of the microfluidic platform from a) perspective, b) top, and c) side view. d) The final realization is represented.

## 2.2. EGOT Fabrication

All the chemicals used for the device fabrication process were purchased from Sigma-Aldrich, unless differently specified.

The devices were fabricated starting from a 4 in. p-type (100) silicon wafer finished with a 1  $\mu\text{m}$   $\text{SiO}_2$  coating (Figure 2a). The AZ 5214E Image Reversal photoresist was used to pattern the gold electrodes through a lift-off process (Figure 2b). After the

UV exposure, a 10 nm thick Ti layer was e-beam evaporated as adhesion layer, followed by a 100 nm thick Au layer deposition (Figure 2c,d). The wafer was then left for 30 min in acetone to remove the photoresist and finalize the electrodes patterning (Figure 2e) and then rinsed with acetone and isopropanol. The obtained transistor channel length and width were, respectively, 10 and 9960  $\mu\text{m}$  (Figure S1, Supporting Information). Another lift-off process was used to pattern a 150 nm thick e-beam

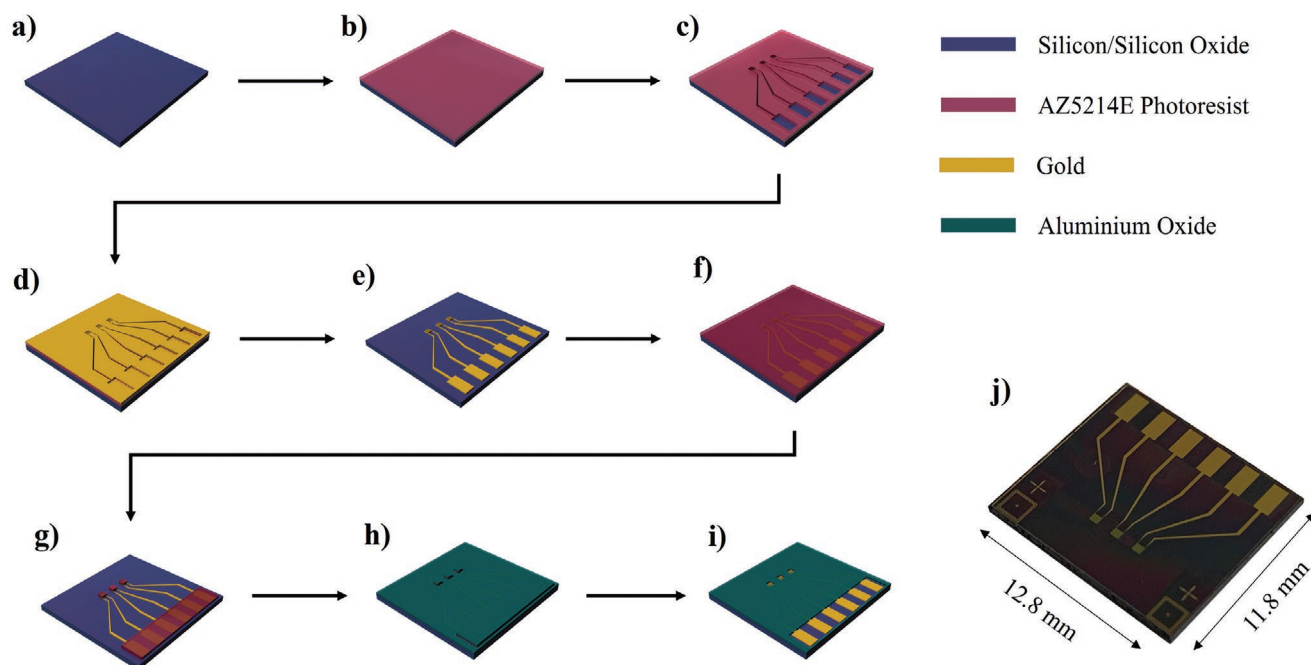


**Figure 2.** The fabrication process consists of two lift-off steps. a–e) The lift-off is used to pattern the gold electrodes, while f–i) it is used to define the passivation layer made of aluminum oxide ( $\text{Al}_2\text{O}_3$ ), which is fundamental to avoid parasitic currents. j) It represented the final chip

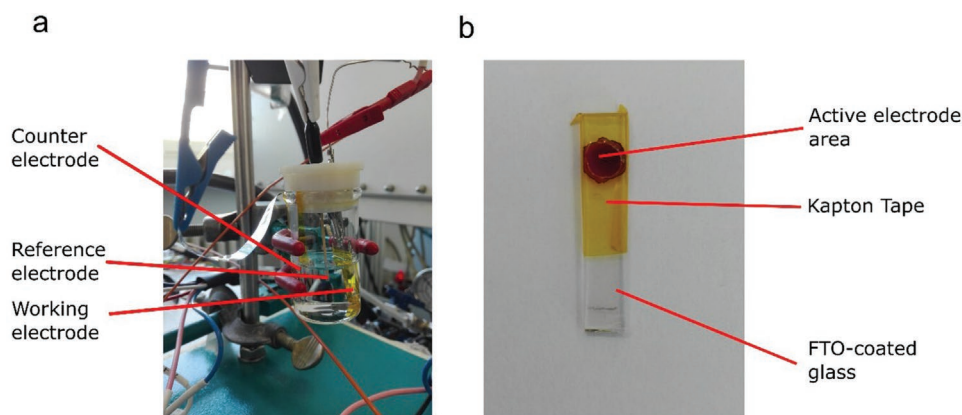


**Figure 3.** a) Electrochemical cell. b) Working electrode with P3HT deposited via drop casting.

evaporated  $\text{Al}_2\text{O}_3$  passivation layer (Figure 2f–i). The wafer was then diced through laser cutting technology (Microla Optoelectronics Srl) to obtain 36 chips out of a single 4 in. wafer (Figure 2j). Each chip was then thoroughly washed in acetone and isopropanol, rinsed, and then kept at 120 °C for 10 min on a hotplate to let any water molecule evaporate.

The gate electrode was obtained by e-beam evaporation of 10 nm of Ti followed by 100 nm of Au onto a silicon oxide-terminated wafer. The latter was then diced through laser cutting in order to obtain single gold plates of dimensions 11.8 mm × 7.8 mm.

The semiconductive polymers used in this work were P3HT and P3CPT, both purchased from Rieke Metals (P3HT:  $M_w = 37$  kDa, regioregularity > 96%; P3CPT:  $M_w = 55$ –65 kDa). P3HT was dissolved in 1,2-dichlorobenzene (oDCB), while P3CPT was dissolved in dimethyl sulfoxide (DMSO), both of them at a concentration of 2.5 mg mL<sup>-1</sup>. From these solutions, the polymers were spin-coated onto the chip at 2000 rpm for 30 s and then annealed in vacuum at 75 °C for 2 h. The final thickness of the polymers was 20 nm for P3HT and 15 nm for P3CPT.

### 2.3. Cyclic Voltammetry

CV was performed with VMP3 potentiostat provided by Bio-Logic. The resolution was 100 μV. Current was integrated over 100% of the resolution step and was averaged over 10 points with a virtual resolution of 1 mV. The upper vertex potential was +1.2 V versus Ag/AgCl and the lower vertex potential was -0.2 V versus Ag/AgCl.

Tetrabutylammonium hexafluorophosphate (provided by Sigma-Aldrich) was dissolved in acetonitrile (99.8% anhydrous provided by Sigma-Aldrich). A 0.1 M solution was prepared in volumetric flask and vortex shaken to ensure complete dissolution.

The electrochemical cell was composed by a 20 mL glass with o-ring sealed 3D-printed cap allowing electrodes setting in still position. A leak-free Ag/AgCl electrode (Innovative Instruments Inc.) filled with 3.4 M KCl was exploited as reference electrode. The leak-free reference electrode was facing the working electrode at fixed distance for repeatable and comparable measurements. The counter electrode was prepared according to

the following procedure: 85 wt% of activated carbon (YP50-F, provided by Kuraray), 10 wt% carbon black (C65, provided by Imerys), and 5 wt% polytetrafluoroethylene (60 wt% water suspension, provided by Sigma-Aldrich) were mixed in rigorous amount of ethanol and let stir in slight boiling condition. The mixture was let stir until the formation of a wet dough. The dough was repeatedly flattened to get a self-standing carbon sheet out of which samples were cut and embodied in aluminum sheet to make a high capacitance electrode. Following this procedure, the counter electrode was virtually nonpolarizing while buffering the experiments' current. The working electrodes were prepared by drop casting of 5 μL of polymer solution (2.5 mg mL<sup>-1</sup> of P3HT in oDCB, or 2.5 mg mL<sup>-1</sup> of P3CPT in DMSO, respectively) on fluorine-doped tin oxide (FTO)-coated glass sheet (provided by Solaronics), followed by 2 h of bake under vacuum at 75 °C. In order to provide comparable measurements, the active area of the working electrodes was limited to a circular window with 5 mm of radius by covering the glass sheets with properly punched Kapton tape. Control measurements were performed on clean FTO-coated glass in order to exclude undesired contributions from the substrate. The electrochemical cell and working electrode are shown in Figure 3.

### 2.4. Device Characterizations

The buffer used for the characterizations was PBS 1× (pH = 7.1), which was provided by a syringe pump connected to the microfluidic platform with a flow rate of 20 μL min<sup>-1</sup> (Figure S2, Supporting Information). The electrical characterizations were performed with a probe station connected to a Keysight B2912A Source/Measure unit and the electrical contacts were ensured by three micromanipulators. The measurements were performed in the common source configuration and the transistors operated in the saturation regime. A schematic representation of the device and the electrical connections is reported in Figure 4.

The figures of merit used in this work were extracted from the  $I_D$ - $V_G$  transfer characteristic of the transistor, that is, the variation of the drain current when sweeping the gate voltage at a fixed drain bias. The  $I_D$ - $V_G$  curves were recorded in the pulse



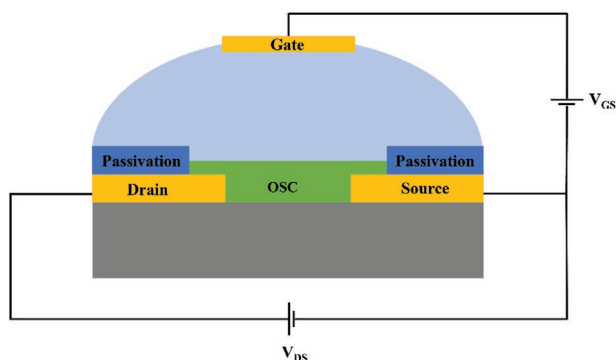


**Figure 4.** Schematic representation of the transistor structure and the electrical connections in the common source configuration.

mode (TPM), following an established protocol which reduced the total amount of EBS.<sup>[16]</sup> In this protocol, both the potentials were provided with pulses of 20 ms, after which they were kept to a base value in order not to stress the transistors. Further details are provided in Figure S3 (Supporting Information). The gate voltage  $V_G$  window was set between 0 and  $-0.6$  V in order to avoid electrolysis phenomena, while the drain voltage  $V_D$  was fixed at  $-0.4$  V. The scan rate of the measurement was  $40 \text{ mV s}^{-1}$ .

The output characteristics of the transistors were recorded by sweeping the drain voltage  $V_D$  from 0 to  $-0.5$  V, while the gate voltage  $V_G$  was kept fixed. This was done for four values of the gate voltage, such as  $V_G = 0, -0.2, -0.4$ , and  $-0.6$  V. The scan rate was  $90 \text{ mV s}^{-1}$ .

The CM was obtained by applying a fixed voltage both at the gate and at the drain electrodes. The voltage values for the gate  $V_G$  and the drain  $V_D$  were, respectively, set to  $-0.6$  and  $-0.4$  V. The CM was applied for almost 16 h and during that time, it was stopped several times to allow the recording of the  $I_D$ - $V_G$  curves, from which it was possible to extract the figures of merit. The transfer curves were sampled at the beginning ( $t = 0$  min) and after 10, 20, 40, 70, 140, 270, 520, and 1000 min. Within the same chip, one device was electrically stressed with the abovementioned protocol, while the other two were left unbiased to allow the quantification of the EBS effects.

For the EBS recovery tests, the devices were stressed with 100 consecutive transfer  $I_D$ - $V_G$  curves in the TPM (for a total of around 50 min of measurement), then let unbiased for 1 h to allow a possible recovery from the EBS, and finally tested with further 100 consecutive transfer curves.

## 2.5. Raman Analysis

Raman spectroscopy was performed with a Renishaw inVia Reflex Raman microscope equipped with a Leica DMLM microscope with a  $50\times$  objective. The sources used for the excitation were a 514.5 and a 785 nm solid state lasers with an output power of 100 mW. All spectra were recorded using 4 accumulations, 20 s exposure, and 5% of the output power. All spectra were recorded in the range between 550 and  $2350 \text{ cm}^{-1}$  when using  $\lambda = 514.5$  nm, and between 600 and  $1700 \text{ cm}^{-1}$  when

using  $\lambda = 875$  nm. The alignment of all spectra was performed by calibration against the  $520.5 \text{ cm}^{-1}$  peak of an internal silicon reference. For each sample presented in the paper, Raman spectra were measured on three different positions in the middle of the transistor channel (i.e., with underlying silicon oxide) and the final spectrum was obtained by averaging the three measurements. This procedure allowed minimizing the influence of film thickness inhomogeneities. In order to allow for a direct comparison between the different samples, all the spectra were finally normalized after removal of the fluorescence baseline.

## 2.6. X-Ray Photoelectron Spectroscopy

XPS measurements were performed using the X-ray source Al K $\alpha$  1486.6 eV, with pass energy 23.50 eV, and take-off angle  $45^\circ$ . In all the spectra, the energy scale was aligned fixing the C1s peak at 284.80 eV. All the peaks were fitted using mixed Gaussian-Lorentzian line shapes (90% Gaussian) and Shirley background, using the  $\Phi$ -Multipak software.

## 3. Results and Discussions

### 3.1. Organic Transistor Characterization

Fundamental characterizations such as  $I$ - $V$  characteristics and CVs were performed in order to assess the functionality of the organic transistors exploited in this work. In order to characterize the polymers and extract the most relevant parameters, CV measurements were performed on the devices (see the Experimental Section for the details). The highest occupied molecular orbital (HOMO) level (relevant for the conduction mechanism of both P3HT and P3CPT) was extracted from the onset potential of the oxidation reaction, by considering the standard potential of Ag/AgCl versus normal hydrogen electrode (NHE) equal to 0.222 V, and the NHE absolute potential of 4.44 V.<sup>[25,26]</sup> Figure 5 shows the CV and chemical structure of P3HT and P3CPT, respectively.

The extracted HOMO levels are  $E_{\text{HOMO}} = -5.13$  eV for P3HT and  $E_{\text{HOMO}} = -5.15$  eV for P3CPT, in accordance with values found in the literature.<sup>[27]</sup> The presence of the carboxyl group in P3CPT side chains have only a minor impact on the position of the HOMO level, which is composed primarily by the  $\pi$ -orbitals of the polymer backbones.

Concerning the  $I$ - $V$  characterizations, transfer ( $I_D$ - $V_G$ ) and output ( $I_D$ - $V_D$ ) were recorded for the two organic transistors using a gold plate as gate electrode, whose results are shown in Figure 6. The measurements were carried out in PBS (measured pH = 7.1) 1 $\times$ . Further details of the measurement protocols can be found in the Experimental Section.

From Figure 6, it is possible to see that both P3HT (Figure 6a) and P3CPT (Figure 6c) transistors work in the saturation regime for  $V_{DS} = -0.4$  V and  $V_{GS} = -0.6$  V, which are the values of drain and gate voltages exploited throughout this work. In addition to this, the transfer curves of the two polymers (Figure 6b,d for P3HT and P3CPT, respectively) show gate leakage currents much smaller (at least two orders

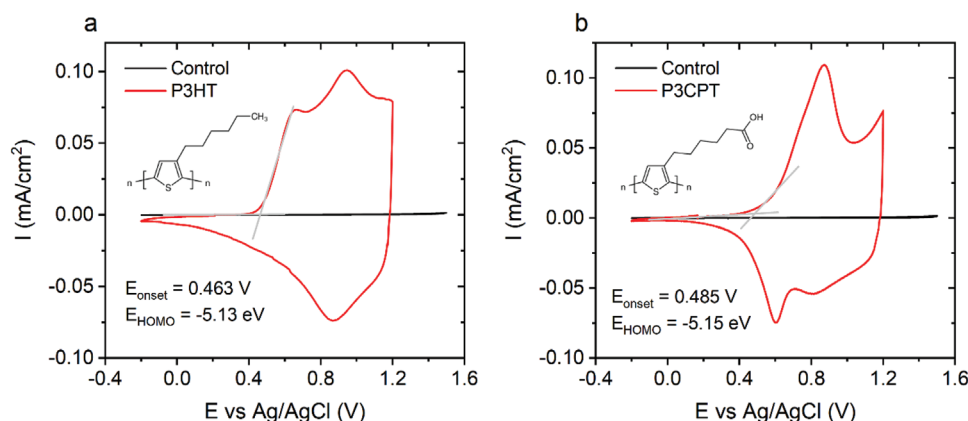


**Figure 5.** Cyclic voltammetry characterization of a) P3HT and b) P3CPT. The HOMO levels of the two polymers have been extracted from the onset potential of oxidation reactions. Insets show the chemical structure of the two polymers.

of magnitude) than the corresponding drain current. It is interesting to notice that P3CPT transistors show greater currents and more pronounced hysteresis than P3HT, which are the typical signs of devices operating in the electrochemical doping regime.

### 3.2. Bias Stress: Continuous Mode

The CM bias stress consisted in the application of a fixed bias at the drain and gate electrodes. The evaluation of devices performance has been performed through the recording of pulsed

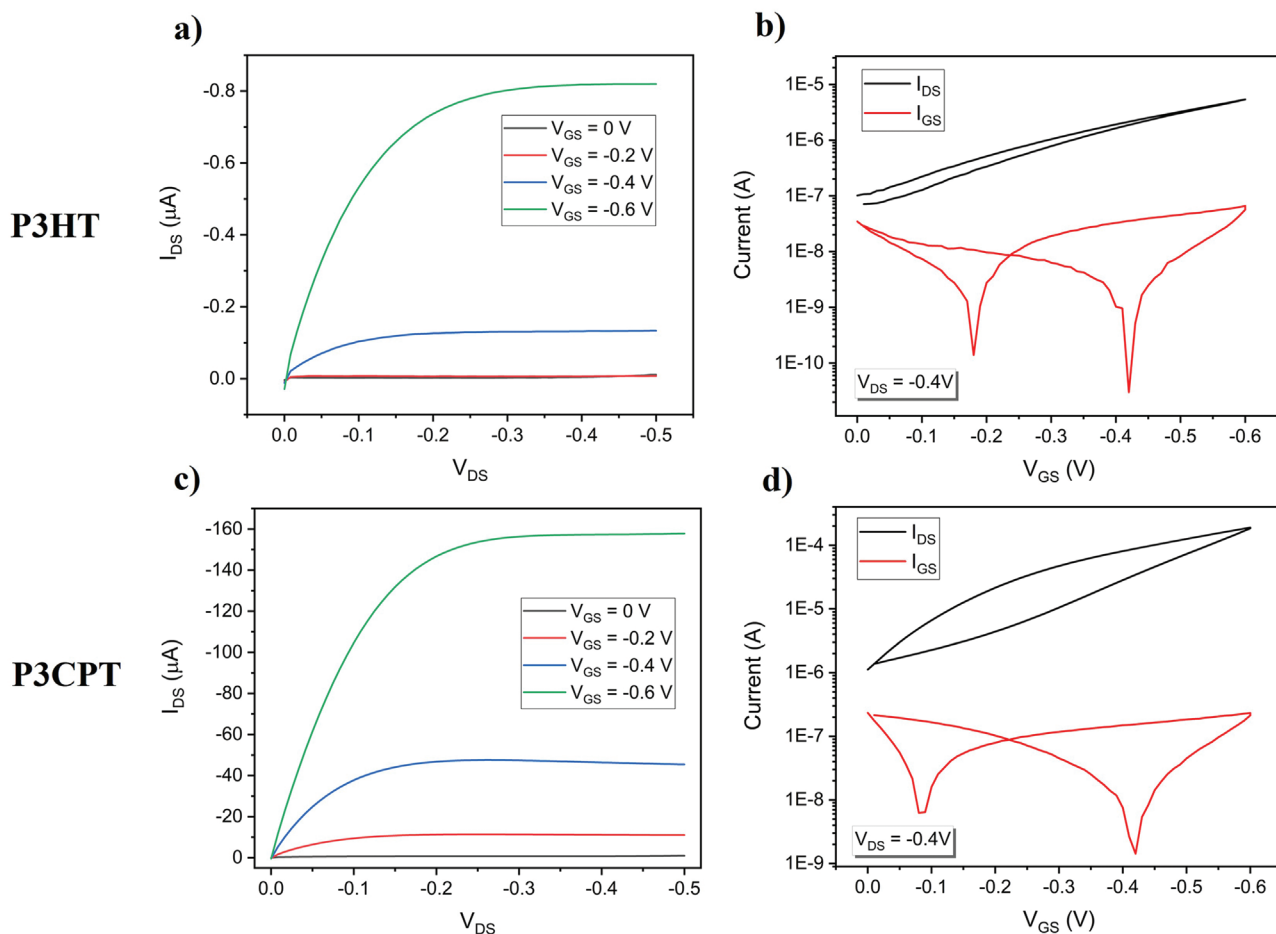


**Figure 6.** Fundamental  $I$ - $V$  characteristics of the organic transistors: a) output curves of P3HT, b) transfer curves of P3HT, c) output curves of P3CPT, and d) transfer curves of P3CPT.

transfer characteristics  $I_D$ – $V_G$  at different time intervals, from which it was possible to extract the relevant figures of merit (see the Experimental Section).

It is important to highlight that the stress introduced with a single pulsed transfer characteristic measurement was negligible compared to the one corresponding to a fixed applied voltage prolonged over time. This is particularly evident by considering that the single  $I_D$ – $V_G$  lasted 15 s and it was run in the pulsed mode, while the constant electrical bias has always been applied for several tens of minutes.

The transfer characteristic curves measured at different times for both the polymers are reported in **Figure 7**. The curves have been normalized to the maximum current of the measurement at  $t = 0$  h to ease the quantification and comparison of the instability of the output current among different devices. The first noticeable result is that the application of a continuous EBS effectively reduces the performances of the devices for both the polymers, resulting as the major source of instability. This is proven through the comparison with the unbiased devices, whose shift

of the maximum current in time is always smaller in value. In particular, for P3HT, the output signal was stabilized after just 1 h from the first measurement when no bias was applied, recording a maximum shift of about –13% (Figure 7a). For the same polymer, the EBS caused a much greater loss of current (–41%) and the stabilization of the signal was not reached in 2 h (Figure 7b). While the EBS was proven to decrease the performances and the stability in P3HT-based devices, the effects on P3CPT are even more detrimental. In fact, without bias, P3CPT showed an increase of the overall performances, with a current growth of 69% in 2 h (Figure 7c). On the contrary, the continuous EBS caused a loss of the maximum current of about –93% in 2 h, which made the tested devices almost impossible to be used further (Figure 7d). It is interesting to notice that the two polymers behave differently in the unbiased case: P3HT reaches a fast stabilization to a lower current value, while P3CPT shows a great increase of the output signal taking more time to reach a stable value. This difference may be ascribed to the different wettability of the two polymers, caused by the different side chains that make

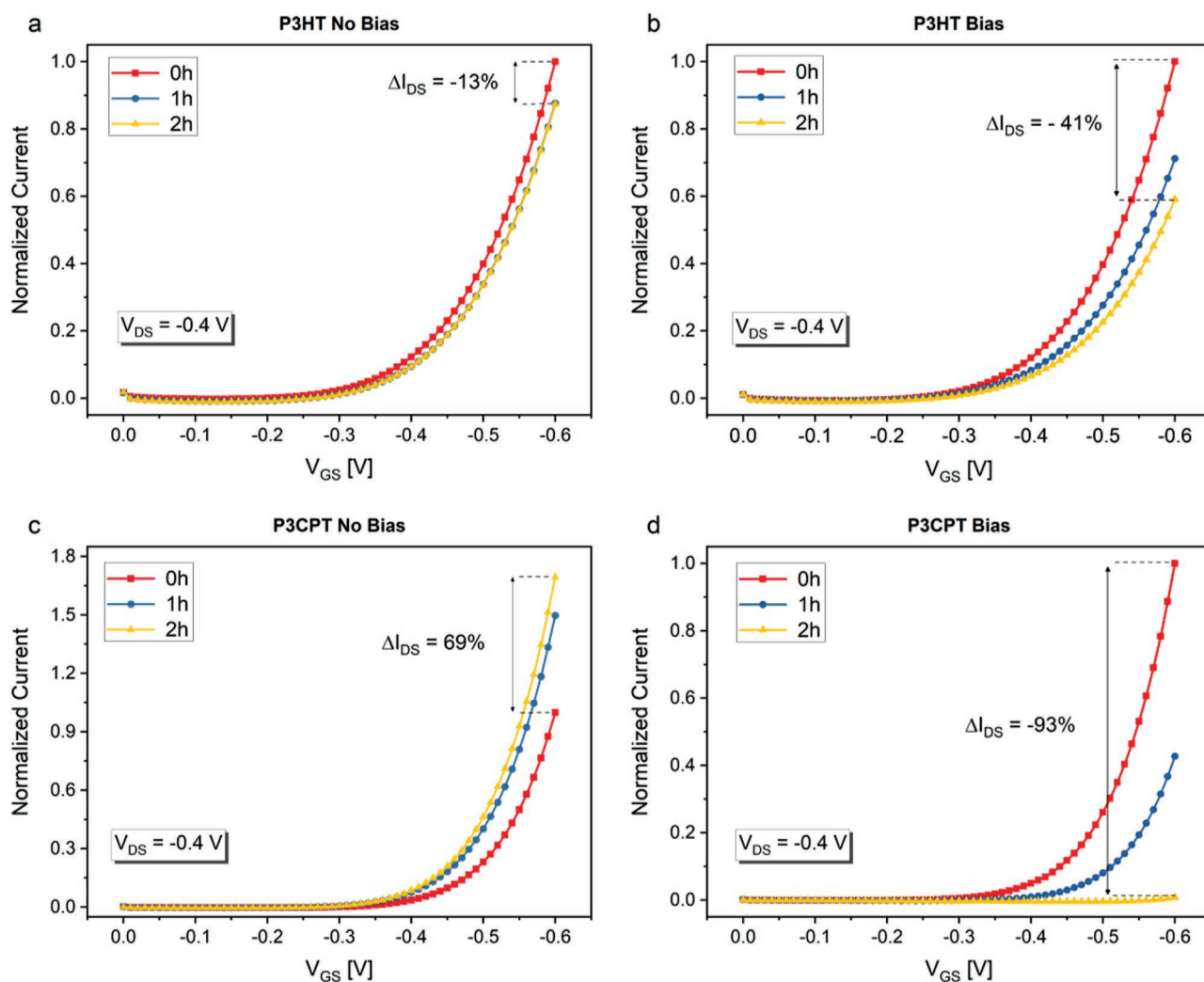


**Figure 7.** Transfer characteristics normalized to the maximum current of the first measure ( $t = 0$  h). In particular, a) represents P3HT unbiased, b) P3HT with bias, c) P3CPT unbiased, and d) P3CPT with bias. For both the polymers, the electrical bias affects the stability of the measurements and decreases the device performance.

P3HT hydrophobic and P3CPT hydrophilic.<sup>[28]</sup> For this reason, P3CPT may be electrochemically doped by the ions present in the electrolytic solution, which could cause the initial increase of the maximum current reported in this work. Similar initial instabilities are found in the literature concerning OECTs and are ascribed to an electrochemical doping induced by the hydration of the organic semiconductor layer.<sup>[29,30]</sup> In P3HT instead, the slight drift during the first phases of the measurements for unbiased devices may be attributed to the hydration of the surface with consequent backbone rearrangement as suggested by the Raman characterizations. The results of XPS characterizations indicate instead that the stronger performance degradation seen in the biased case may be ascribed to an EBS-induced oxidation of the most superficial polymer layer, resulting in a degradation of charge carrier mobility (see Sections 3.3 and 3.4 for the details concerning Raman and XPS analyses).

In order to better understand the mechanisms that govern the instability in these two polymers, an analysis involving 26 devices was conducted on the threshold voltage ( $V_T$ ) and transconductance ( $G$ ) shift over time, with and without bias applied (Figure 8). For P3HT, the results showed that the threshold voltage was almost unaffected by the EBS, resulting

in a slight shift on its mean value with greater standard deviations compared to the unbiased case (Figure 8a). On the other hand, the maximum transconductance ( $G_{\max}$ ) presented a significant variation (Figure 8b), with a maximum shift within 2 h from the first measurement increased from about 10% without bias to almost 40% with bias, confirming the first measurements reported in Figure 7. It is important to highlight that after almost 16 h of measurements, both the  $V_T$  and the  $G_{\max}$  decreased for P3HT independently on the applied bias. This may be ascribed to the intercalation of water molecules in the polymer film after prolonged exposure to the aqueous electrolyte, with a consequent decrease of the hole mobility.<sup>[31,32]</sup>

For P3CPT, the analysis confirmed the detrimental effect of the EBS over the polymer behavior. In particular, the absolute value of the  $V_T$  continuously increased because of the bias stress, which consequently made the transistor always more difficult to switch-on for the same applied gate voltage (Figure 8c). In addition, a high dispersion of the  $V_T$  values versus time was registered among different devices subjected to bias stress, which is reflected by the higher standard deviations compared to ones of the reference devices. The same happened for the  $G_{\max}$ , which tended to decrease logarithmically over time (Figure 8d).

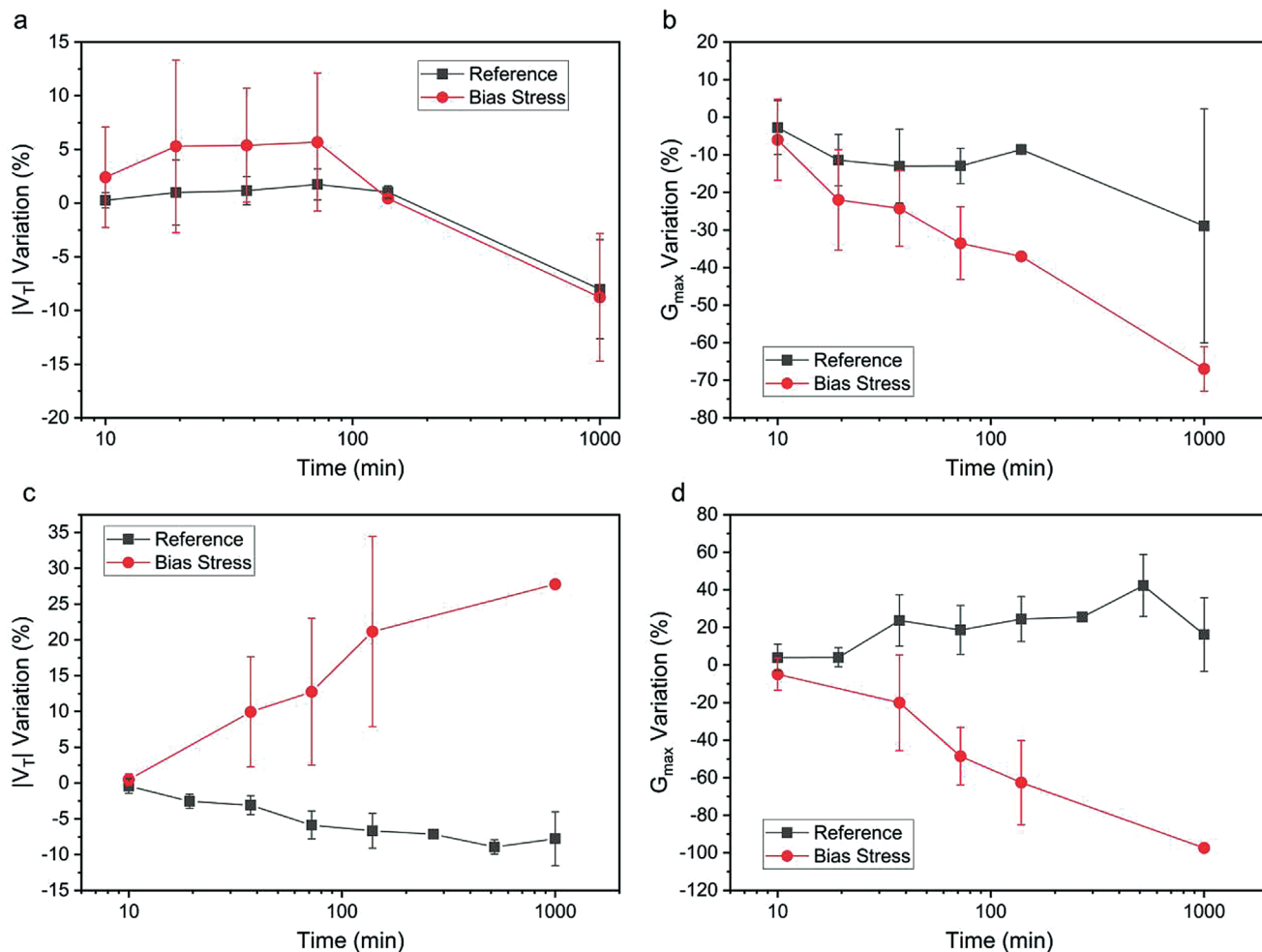


**Figure 8.** Effect of the electrical bias stress on a,b) P3HT and c,d) P3CPT EGOT-based figures of merit. All the values are normalized to the first one to have a clearer view of the instabilities. The data were collected with  $V_{DS} = -0.4$  V and  $V_{GS}$  sweeping from 0 to  $-0.6$  V.



**Table 1.** Figures of merit ( $V_T$  and  $G_{\max}$ ) variations depending on the EBS in time.

	No bias		Bias		
Max $\Delta V_T $ [%]	2	−7	6	21	After 2 h
Max $\Delta G_{\max}$ [%]	−12	25	−37	−62	—
Max $\Delta V_T $ [%]	−8	−9	−9	28	After 16 h
Max $\Delta G_{\max}$ [%]	−29	42	−67	−97	—
	P3HT	P3CPT	P3HT	P3CPT	

The impact of the EBS on P3CPT-based transistors was also investigated for different pH values in order to evaluate the effects of a possible deprotonation of the carboxyl groups induced by the EBS. The chosen pH ranged from 6 to 8 in order to guarantee the buffering capability of the PBS buffer.<sup>[33]</sup> Within these pH values, there was not a significant trend in the transistors figures of merit when moving from an acidic buffer to a basic one, as reported in Figure S4 (Supporting Information). The lack of correlation between pH and the effects of the electrical bias stress suggests that deprotonation of the carboxyl groups does not play any role, which is in agreement with low acid dissociation constant of carboxyl groups ( $pK_a = 4.2$ ).<sup>[34]</sup>

From the collected data, it is evident that the effect of bias stress is different in the two materials, with a stronger performance degradation for the P3CPT, as summarized in Table 1. In particular, the EBS had a minor impact on P3HT, which seemed just to accelerate the polymer degradation process that causes a drop of hole mobility (and therefore of transconductance). Conversely, in P3CPT, the EBS had a dramatic impact on the transistor behavior, which changed completely in the absence of an electrical stress (the transconductance increased without bias, while it dropped with bias).

These experiments also demonstrate that the stabilization dynamics is different for the two polymers when unbiased. In fact, in P3CPT, the stability was reached at least 2 h after the contact with the electrolyte, while for P3HT, the stabilization was much faster with a tendency to slightly decrease its

performances over long period of time, as previously discussed. These results highlight the importance of designing polymer-dependent stabilization protocols, which are fundamental in biosensing applications to improve the performances and avoid deceptive results.

### 3.3. Raman Spectroscopy

Resonant (excitation wavelength  $\lambda = 514.5$  nm) and nonresonant (excitation wavelength  $\lambda = 785$  nm) Raman characterizations have been carried out on three sets of devices: as prepared and stored in vacuum (Vacuum samples), devices stored in PBS 1× without application of any bias (No bias samples), and devices stored in PBS 1× after application of a continuous bias for 3 h (Bias samples). This allowed assessing the influence both of the exposure to an aqueous electrolyte and of the application of a bias stress on the two polymers. It is well-known that the wavelength  $\lambda = 514.5$  nm is best suited for the resonant excitation of Raman C—C and C=C lines coming from neutral undoped and nonoxidized portions of polythiophene chains, while longer wavelengths can be exploited to obtain structural information about both neutral and oxidized species simultaneously.<sup>[35–37]</sup>

In Figure 9a, the Raman spectra of P3HT and P3CPT measured on Vacuum samples with excitation wavelength  $\lambda = 514.5$  nm are shown. Seven main features can be distinguished and are attributed to different vibrational bands in P3HT spectra. The low intensity peak at  $1510\text{ cm}^{-1}$  is assigned to C=C antisymmetric vibrations in the thiophene rings.<sup>[36,37]</sup> The high intensity band at  $1443\text{ cm}^{-1}$  is instead attributed to symmetric C=C stretching deformations, while the peak at  $1376\text{ cm}^{-1}$  is due to C—C stretching deformation in the thiophene ring.<sup>[36,37]</sup> These last two bands are associated to conjugated polythiophene segments in the neutral state, and their intensity is resonantly enhanced by  $\lambda = 514.5$  nm.<sup>[35]</sup> The two weaker features at  $1206$  and  $1179\text{ cm}^{-1}$  can be assigned, respectively, to C—C interring symmetric stretching and C—H bending.<sup>[36,37]</sup> A small feature centered around  $1166\text{ cm}^{-1}$  (not indicated in Figure 9a)

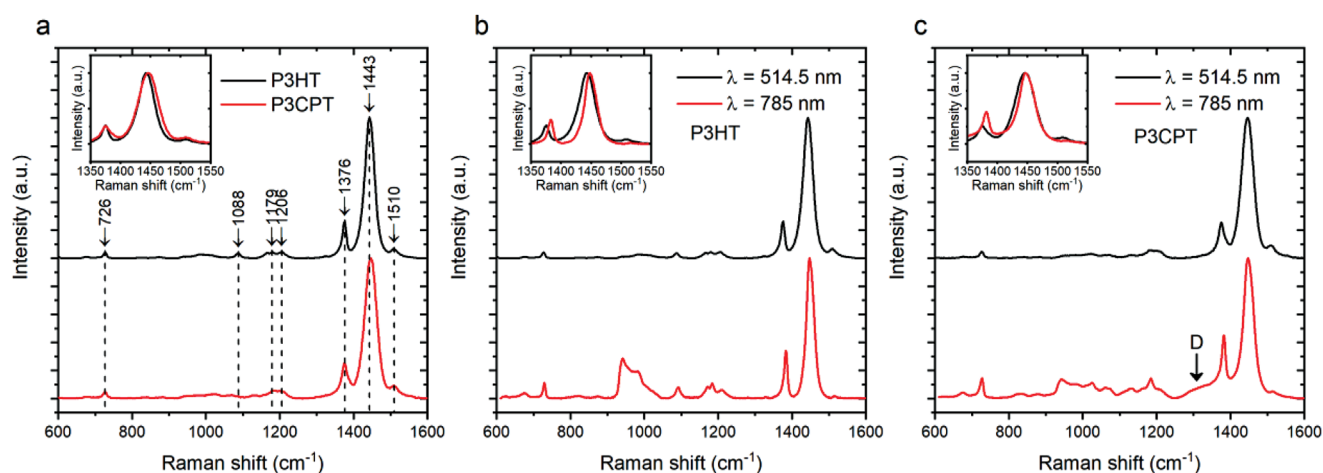


**Figure 9.** a) Comparison between P3HT and P3CPT normalized Raman spectra measured with excitation  $\lambda = 514.5$  nm on Vacuum samples. Assignments of the peaks is discussed in the main text. b) Comparison of normalized Raman spectra of P3HT Vacuum samples measured with excitation  $\lambda = 514.5$  nm and  $\lambda = 785$  nm. c) Comparison of normalized Raman spectra of P3HT Vacuum samples measured with excitation  $\lambda = 514.5$  nm and  $\lambda = 785$  nm. Insets show a zoom on the  $1350\text{--}1550\text{ cm}^{-1}$  regions.

may be attributed to the presence of the alkyl side chain.<sup>[38]</sup> This feature is present in P3HT spectra but not in P3CPT, therefore we tentatively attribute the peak to the presence of nonpolar methyl group in P3HT side chains, which are replaced by polar carboxyl groups in P3CPT. The feature at 1088 cm<sup>-1</sup> is again assigned to C–H bending.<sup>[39]</sup> Finally, the low intensity bands at 726 and 678 cm<sup>-1</sup> (not indicated) are assigned to C–S–C ring deformations.<sup>[36,37,39]</sup>

The two main peaks at 1443 cm<sup>-1</sup> (C=C symmetric stretching) and 1376 cm<sup>-1</sup> (C–C intraring stretching) can be used to obtain information about the degree of  $\pi$ -electron delocalization and structural order of the film.<sup>[40,41]</sup> As can be noted from the inset of Figure 9a, in P3CPT, both these bands present a broader full width at half maximum (39.2 and 24.1 cm<sup>-1</sup> for the C=C and C–C bands, respectively) compared to P3HT (31.7 and 14.1 cm<sup>-1</sup>, respectively). Moreover, the C=C band of P3CPT results shifted toward higher wavenumbers, being centered at 1446 cm<sup>-1</sup> (see Table S1 in the Supporting Information). The sharper and redshifted peaks of P3HT indicate the presence of longer conjugation length with planar chains and higher crystallinity of the film.<sup>[42]</sup>

Nonresonant Raman characterizations with excitation wavelength  $\lambda = 785$  nm have been performed in order to investigate the presence of defects and oxidized distorted chains in pristine (Vacuum) samples. As can be noted from Figure 9b, the only additional feature present in P3HT spectrum measured at  $\lambda = 785$  nm is a broad band around 970 cm<sup>-1</sup>, assigned to Si–OH vibrations coming from the SiO<sub>2</sub> underlying the organic semiconductor.<sup>[43]</sup> A relative enhancement of the low intensity bands compared to the main one is also obtained, as expected for neutral polymer measured in nonresonant condition. On the other hand, P3CPT spectrum measured with  $\lambda = 785$  nm (see Figure 9c) presents additional broad shoulders and kinks that are not visible at the shorter wavelength, which can therefore be associated to oxidized and distorted polymer chains. A partial oxidation of P3CPT Vacuum sample has been found also from XPS characterization, and it may be ascribed to the polymer synthesis process. The main shoulder attributed to the presence of disorder in the film is labeled D in Figure 9c. A similar shoulder has been reported in the literature for different oxidized and p-type doped substituted polythiophene, and we attribute the presence of these defects to conformational disorder arising from twisted P3CPT backbones.<sup>[35,36,39,44]</sup> A detailed discussion about the origin of this peak is provided later on in the text.

As already mentioned, the wavelength  $\lambda = 514.5$  nm can only probe the neutral undoped and nonoxidized portions of polythiophenes chains.<sup>[35–37]</sup> Raman spectra of the two polymers measured on the different samples (Vacuum, No bias, and Bias) at  $\lambda = 514.5$  nm indeed do not present any major difference. As can be seen in Figure S5 and Table S1 (Supporting Information), only a shift of 2 cm<sup>-1</sup> toward higher wavenumber is measured in the spectra of the two polymers when exposed to the aqueous electrolyte (No bias and Bias samples) compared with the one stored in vacuum, accompanied by a small decrease in relative intensity of the C–C intraring band in P3CPT. This shift can be attributed to a slight rearrangement of polymer backbones induced by the contact with water, which may be responsible for instabilities measured also in No bias samples (see Figures 7 and 8).

Nonresonant Raman characterizations have been exploited to investigate the occurrence of electrochemical doping and oxidative processes taking place during bias stress measurements. In Figure 10a,b is reported the spectra of P3HT and P3CPT, respectively, measured in the three different conditions (i.e., Vacuum, No bias, and Bias). The spectra of P3HT shown in Figure 10a present no differences each other, therefore indicating no or negligible oxidation and electrochemical doping of the polymer up to 3 h of bias stress measurement. On the other hand, clear signs of polymer oxidation/doping are present in Figure 10b in the spectrum of P3CPT samples exposed to water, similarly to those previously observed in different substituted polythiophenes subjected to oxidative doping.<sup>[36,39,44,45]</sup> Briefly: a redshift and broadening of the main C=C components is accompanied by a relative increase of the C–S–C band (727 cm<sup>-1</sup>), of the inter-ring C–C band (1205 cm<sup>-1</sup>), and of the intraring C–C peak (1382 cm<sup>-1</sup>), as summarized in Table S1 (Supporting Information). More specifically, the increase of inter-ring C–C band and C–S–C band are commonly associated to the formation of polaronic species that induce torsional disorder along the polymer backbones.<sup>[39,40,44]</sup> In order to better understand the degradation of charge transport properties of the polymer, we focused on the region between 1300 and 1500 cm<sup>-1</sup>, where the bands sensitive to the  $\pi$ -electron delocalization lie. Figure 10c–e shows the deconvolution of the region of interest, respectively, for Vacuum, No bias, and Bias P3CPT samples. In order to fit the Vacuum spectrum, three Lorentzian and one Gaussian components have been used. Two Lorentzian components have been exploited to fit the C=C band, centered around 1440 and 1460 cm<sup>-1</sup> and associated, respectively, to aggregated (C=C<sup>agg</sup>) and unaggregated (C=C<sup>un</sup>) bonds.<sup>[41,42]</sup> The C–C intraring band has been fitted with the third Lorentzian component around 1380 cm<sup>-1</sup>. The appearance of a Gaussian component (*D*) on the low-energy wing of the Raman profile (in our case centered around 1350 cm<sup>-1</sup>) implies the presence of disorder and inhomogeneity in the film.<sup>[39]</sup> A more disordered film is expected for P3CPT compared to P3HT due to its lower regioregularity and higher molecular weight.<sup>[46]</sup> Upon exposure of the samples to the aqueous electrolyte (Figure 10d), a novel Lorentzian component (C=C<sup>quin</sup>) arises around 1430 cm<sup>-1</sup>. A detailed Raman characterization of P3CPT is still remarkably lacking in the literature, however the appearance of a band around 1430 cm<sup>-1</sup> has been previously observed in the literature concerning P3HT. This has been associated to an increase of conformational disorder induced by a number of different mechanisms like the formation of charge transfer complexes with molecular oxygen and dopant anions, neutron radiation damaging, and order/disorder transition resulting from the polymer oxidation to its quinoid form.<sup>[37,39,40,44]</sup> As can be noted in Figure 10e, both this peak and the Gaussian component associated to disorder in the film increase after application of a bias stress. Considering these results, we ascribe the degradation of P3CPT electronic properties to an increase of disorder in the film described in terms of formation of polaronic species which disrupt chains coplanarity when these chains are oxidized to their quinoid state. Since this effect is not visible in P3HT measured under the same conditions, we can infer that the carboxypentyl side chains play a prominent role in P3CPT degradation. The

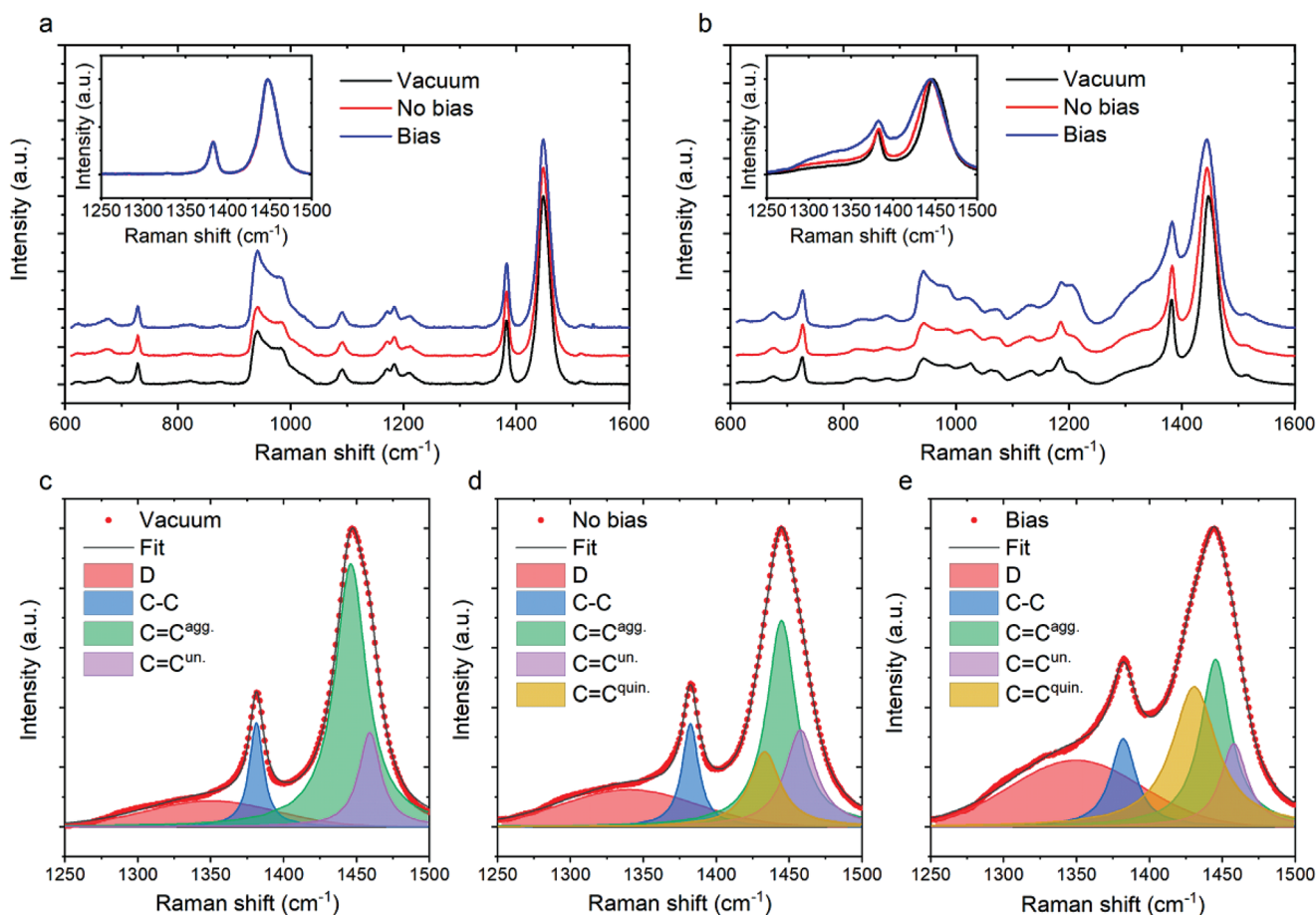


**Figure 10.** a) Comparison of Raman spectra measured with  $\lambda = 785$  nm in Vacuum, No bias, and Bias P3HT samples. b) Comparison of Raman spectra measured with  $\lambda = 785$  nm on Vacuum, No bias, and Bias P3CPT samples. c–e) Peak deconvolution of P3CPT Vacuum, No bias, and Bias samples, respectively.

polar nature of these chains in fact allows for an easier penetration of water molecules and ions inside the film, thus promoting oxidation processes as well as steric-hindrance-induced deformations of the backbones. Moreover, the deprotonation of carboxyl groups to carboxylate anions may emphasize the formation of polaronic countercharges on adjacent backbones, further increasing molecular distortion.

### 3.4. X-Ray Photoelectron Spectroscopy

XPS analysis has been performed on P3HT-based EGOFETs and on P3CPT-based OECTs, before electronic characterizations (Vacuum samples) and after bias stress applied in CM (Bias samples). This characterization allowed investigating with high resolution the topmost superficial layer of the films. Measurement details are provided in the Experimental Section.

The C1s peak measured on the Vacuum sample (Figure 11a, top panel) can be deconvoluted with three components at binding energy (B.E.) 284.29, 284.84, and 285.50 eV, respectively, accounting for C=C bond atoms in the thiophene ring, C–C bonds in the alkyl side chains, and C–S bonds in the thiophene ring, with relative area 1:3:1 to account for the molecular structure of P3HT.<sup>[47–49]</sup> After Bias stress measurement,

the C1s peak presents a new feature on the high binding energy side (Figure 11a, bottom panel), which can be fitted with a component centered at 286.30 eV attributed to C–OH bonds (see Table S2 in the Supporting Information for the details). The appearance of this new component, combined with the decrease in relative area associated to C–C bonds can be ascribed to the oxidation of  $\alpha$ -carbon in the hexyl groups, with consecutive cleavage of the polymer side chains.<sup>[48,50,51]</sup> These results suggest that the degradation of performances seen in P3HT-based EGOFETs could be ascribed to a loss of conjugation along the polymer backbone caused by conformational defects resulting from alkyl side chains' oxidation, with consequent loss of interchain  $\pi$ – $\pi$  stacking, similarly to what has been previously reported by Jeong et al.<sup>[31]</sup>

The C1s of P3CPT Vacuum and Bias samples are shown in Figure 11b. The C1s peak of P3CPT Vacuum (Figure 11b, top panel) presents two additional components compared to P3HT. The feature at higher B.E. is related to the terminal carboxyl groups of the side chain (B.E. 289.52 eV). A second shoulder at 286.50 eV indicates the presence of C–OH bonds.<sup>[48]</sup> A similar shoulder has been previously reported in the literature for P3CPT obtained via carboxylic acid functionalization of poly(3-(potassium-4-butanoate)thiophene-2,5-diyl), therefore we ascribe the presence of this feature in Vacuum samples to the

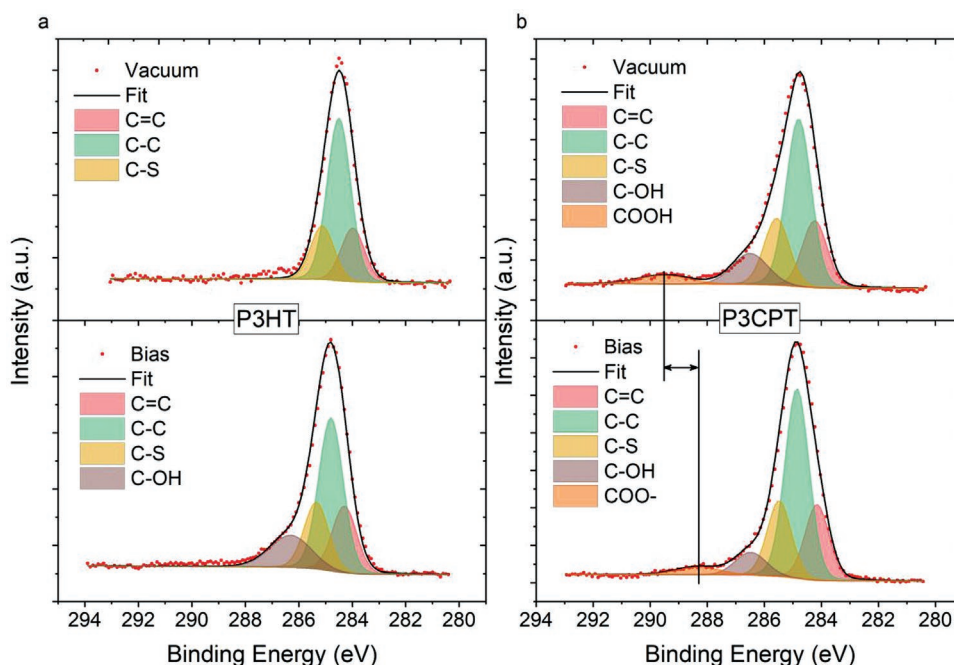


**Figure 11.** a) C1s peak of P3HT Vacuum sample (top panel) and Bias sample (bottom panel). b) C1s peak of P3CPT Vacuum sample (top panel) and Bias sample (bottom panel). The fitting parameters of the deconvolution components are detailed in Table S2 (Supporting Information).

synthesis of the polymer.<sup>[22]</sup> In Bias sample, the peak associated to COOH groups results shifted at lower B.E. (B.E. 288.30 eV), as can be noted from the bottom panel of Figure 11b and Table S2 (Supporting Information). This shift to lower B.E. is in agreement with those found in the literature upon deprotonation of carboxylic acids.<sup>[52,53]</sup> The arise of oxidative components after bias stress measurement was also verified by the high resolution XPS analysis of S2p peak, as discussed in Table S3 and Figure S6 (Supporting Information).

### 3.5. Bias Stress: Pulsed Transfer Mode and Physical Model

A further experiment was carried out to investigate the effects of the EBS when consecutive transfer curves are recorded on the devices in the TPM. Thus, differently from the previous tests, the bias stress was not applied through a fixed bias voltage, but it was imposed through two sets of transfer curves measurement (100 curves for each set), with 1 h pause between the sets. This made possible to monitor almost continuously (every 15 s) the variation of the two figures of merit under study (i.e., threshold voltage and maximum transconductance). The bias pause of 1 h between the first and the second set of transfer curves was introduced to investigate the presence of a spontaneous recovery mechanism that could restore the devices output. The results of this experiment are visible in Figure 12, which shows an opposite behavior between the two polymers. In fact, for P3HT, there is an almost full recovery of the figures of merit after the bias break, while for P3CPT, it is demonstrated that neither the threshold voltage nor the  $G_{\max}$  recover the initial values. Thus, there is a bias memory effect in P3CPT that is not present in P3HT, as evidenced in Table 2. It is also interesting to notice the presence of polarization

effects at the beginning of the second set of measurements, which induce a slight shift of the values with respect to the main trend.

To assess the origins of this bias memory effect in P3CPT, a mathematical model is here proposed based on a stretched exponential function, which has been demonstrated to be well suited for the description of the EBS-driven instability phenomena in solid insulating dielectric OFETs.<sup>[54,55]</sup>

Concerning P3CPT, the threshold voltage experimental data were fitted according to the following equation (Equation (1))<sup>[13]</sup>

$$V_T(t) = V_0 \left\{ 1 - \exp \left[ - \left( \frac{t}{\tau} \right)^\beta \right] \right\} + c \quad (1)$$

where  $V_0$  is the asymptotic voltage threshold value,  $\tau$  is the relaxation time,  $\beta$  the dispersion parameter related to trap states, and  $c$  a constant. Based on this model, the relaxation time can be seen as the average time before a charged carrier is trapped due to the EBS, while the dispersion parameter  $\beta$  represents the width of the distribution in energy of the trap sites.<sup>[56,57]</sup> The fit of the first 100 consecutive  $I_D$ - $V_G$  curves for P3CPT (Figure 13) revealed that this model describes accurately the variations of the threshold voltage also for aqueous electrolyte-gated organic transistors, with an adjusted  $R$ -square of 0.9995. The extracted parameters values are  $\tau = 326$  s for the relaxation time,  $\beta = 0.619$  for the dispersion parameter,  $V_0 = -0.179$  V for the voltage prefactor and  $3.3 \times 10^{-2}$  V for the constant term. From a comparison with the existing literature, it results that the dispersion factor is similar to the one of a solid-state gated P3HT transistor, which suggests that the trap density may not be affected by the presence of the electrolyte rather than a solid



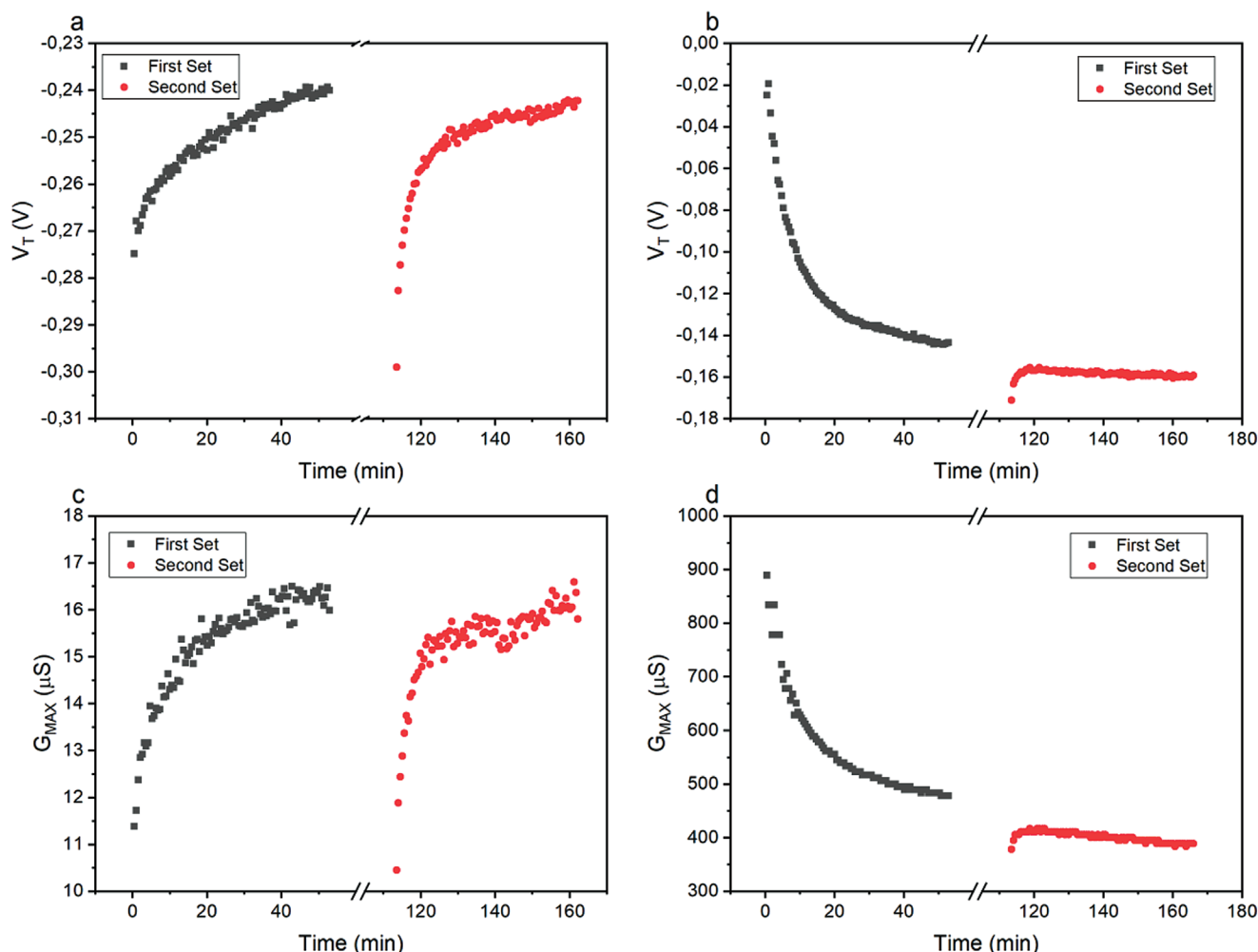


**Figure 12.** Figures of merit recovery. a,c) P3HT recovered completely after 1 h, while b,d) P3CPT kept memory of the previously applied bias. For these measurements  $V_{DS} = -0.4$  V, while  $V_{GS}$  was swept from 0 to  $-0.6$  V (TPM).

dielectric.<sup>[58]</sup> Conversely, the extracted relaxation time is much smaller than the one found for solid-state transistors, but similar to the case in which the device is gated through a polyelectrolyte.<sup>[55,59]</sup> Thus, it seems that the presence of the electrolyte accelerates the filling of trap states, which may be associated to the different ion mobility between the electrolytic and the insulating gating material. These things considered, despite the EBS-driven instability mechanisms may be due to different physical phenomena, this result demonstrates that the mathematical model still holds for P3CPT-based EGOTs.

**Table 2.**  $V_T$  and  $G_{max}$  values at the beginning and at the end of 100 repetitions of transfer curves.

	P3HT		P3CPT	
$V_T$ start [mV]	−270	−300	−19	−171
$V_T$ end [mV]	−240	−242	−143	−159
$G_{max}$ start [ $\mu$ S]	11	10	888	378
$G_{max}$ end [ $\mu$ S]	16	16	478	389
	1st set	2nd set	1st set	2nd set

In order to further validate the model, the same parameters were used to fit with Equation (1) also the second set of measurement of P3CPT. It is possible to see (Figure 13b) that the model does not describe accurately the variations in the long-term range. The actual threshold voltage shift is in fact greater than the one described by the function, which means that other processes than the EBS occur. In particular, the overall threshold voltage variation may be ascribed both to the EBS effect (modeled with a stretched exponential function) and to a change of the polymer properties that is independent to the applied bias, as visible from the fact that a slow drift is present during the recovery phase as well. In the saturation region, the output current of the EGOT can be written according to Equation (2)

$$I_{DS} = \frac{W}{2L} \alpha (V_{GS} - V_T)^2 \quad (2)$$

where  $W$  and  $L$  are, respectively, the width and the length of the transistor channel and  $\alpha$  is the product of the carriers mobility  $\mu$  and the total system capacitance  $C$ , which is the series of the OSC/electrolyte and electrolyte/gate electrode capacitances.<sup>[60]</sup> According to Equation (2), the two figures of merit studied in

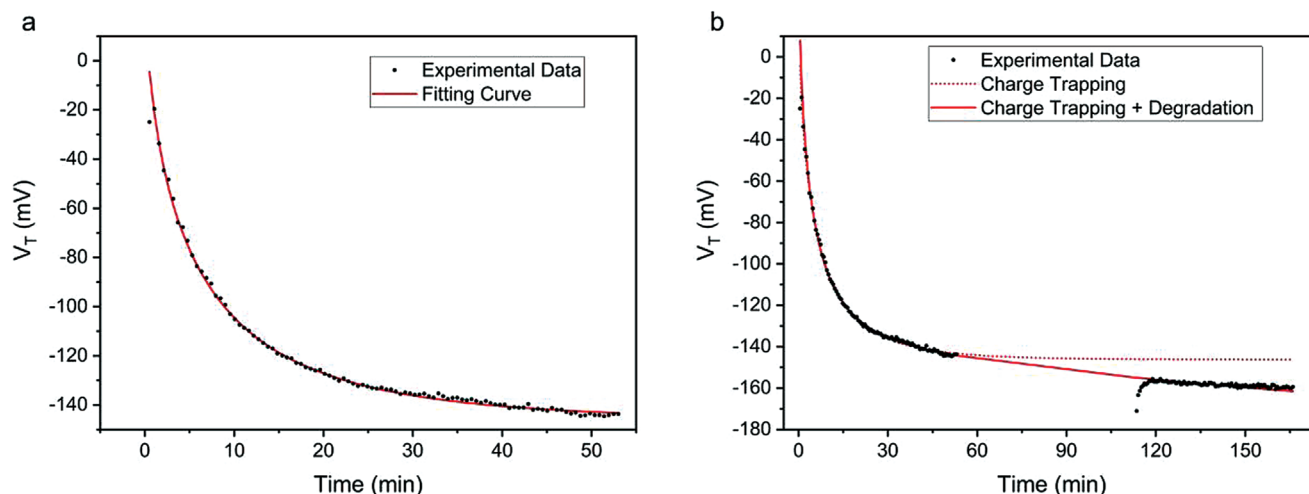


**Figure 13.** Threshold voltage change over time for P3CPT. a) The first set of measurements is fitted with a stretched exponential function. b) The two sets of measurements are fitted with the stretched exponential (dotted red line) and with a combined function accounting for the polymer degradation (solid red line). For these measurements  $V_{DS} = -0.4$  V, while  $V_{GS}$  was swept from 0 to  $-0.6$  V (TPM).

this work (threshold voltage and maximum transconductance) can be calculated as

$$V_T = V_{GS} - \sqrt{\frac{2L}{W\alpha}} \sqrt{I_{DS}} \quad (3)$$

$$G_{\max} = \max\left(\frac{\partial I_{DS}}{\partial V_{GS}}\right) = \max\left(\frac{W}{L} \alpha (V_{GS} - V_T)\right) \quad (4)$$

Assuming that the polymer electronic properties (i.e., charge carriers mobility and capacitance) do not change over time, the maximum transconductance  $G_{\max}$  should be dependent on time through the sole variation of the threshold voltage  $V_T$ , being all the other parameters constant. Thus, from the first  $I_D$ - $V_G$  curve, it was possible to extract the  $\alpha$  parameter, which was then exploited to calculate the maximum transconductance shift given by the threshold voltage change, i.e., with constant  $\alpha$  and exploiting the experimental values of  $V_T$ . It was found that the experimental value of the maximum transconductance was lower than the theoretical one, implying that  $G_{\max}$  is dependent on time not only through  $V_T(t)$  but also through the parameter  $\alpha(t)$ , which decreases almost linearly in time (Figure S7, Supporting Information). This further effect should be taken into account in the mathematical model of the threshold voltage. In fact, Equation (3) shows that  $V_T$  depends on the factor  $\alpha$  under square root, whose effects are not considered in the stretched exponential-based model. Thus, we here propose a new equation for the mathematical model to describe the variation of the threshold voltage in electrolyte-gated OFETs accounting for both the charge trapping and the polymer degradation phenomena. This new function can be written as

$$V_T(t) = V_0 \left\{ 1 - \exp\left[-\left(\frac{t}{\tau}\right)^\beta\right] \right\} - \sqrt{\gamma t} + c \quad (5)$$

where  $\gamma$  is a constant taking into account the variation of the  $\alpha$  parameter previously discussed.

Exploiting Equation (5) to fit the whole set of measurement of P3CPT, the result was more accurate, with an adjusted

R-square value of 0.9993 (Figure 13b). The extracted parameters are summarized in Table 3 for an easier comparison with the first fit presented.

It is important to notice that the values of the parameters related to the stretched exponential function are consistent within the two fits presented, which is a further proof of the accuracy of the model of the threshold voltage variation presented for P3CPT-based EGOTs. Interestingly, the stretched exponential function was accurately modeling the first set of measurements even if the model was not taking into account the polymer degradation. We ascribe this result to the fact that, at the beginning, the major contribution comes from the EBS-induced trapping of free carriers, which makes the second contribution almost negligible. However, once the major contribution of the EBS vanishes (after  $5\tau$ , the change of  $V_T$  is around 90% of the total drift), the square root dependence becomes the predominant factor and must be then taken into account. Another interesting aspect is that the combined function describes accurately the whole measurements for P3CPT despite between the first and the second set there is a pause in the EBS application of 1 h. This can again be ascribed to the different timescales of the two drift mechanisms. In fact, after the first set (lasting 50 min), the majority of the EBS effects are extinguished and the polymer drift becomes the sole mechanisms playing an active role. The

**Table 3.** Fit parameters for the stretched exponential function of the first set and the combined (stretched exponential with square root dependence) function of the two sets of measurements of P3CPT.

P3CPT	Stretched exponential (1st set)	Stretched exponential (1st + 2nd sets)	Combined function (1st + 2nd sets)
$V_0$ [mV]	-179	-179	-179
$\tau$ [s]	326	326	223
$\beta$	0.619	0.619	0.630
$c$ [mV]	33	33	55
$\gamma$ [V <sup>2</sup> s <sup>-1</sup> ]	—	—	$1.4 \times 10^{-7}$
Adj. R-square	0.9995	0.8769	0.9993

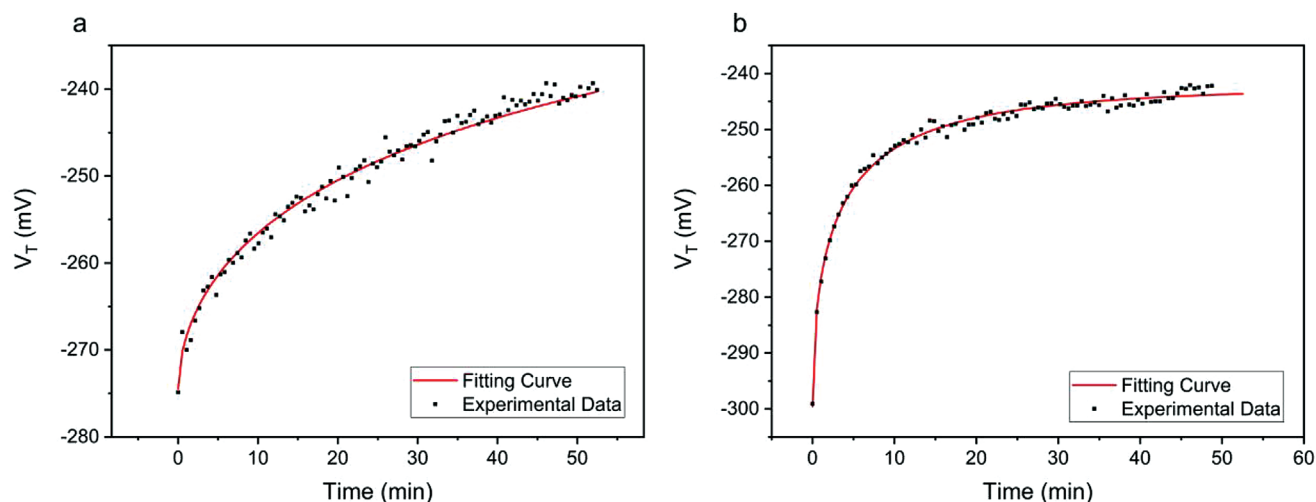


**Figure 14.** Threshold voltage change over time data for P3HT with the stretched exponential function fit for a) the first and b) the second set of measurements. For these measurements  $V_{DS} = -0.4$  V, while  $V_{GS}$  was swept from 0 to  $-0.6$  V (TPM).

same analysis of the fit was performed for the  $I_D$ - $V_G$  measurements on P3HT. Even in this case, the threshold voltage variation was modeled with a stretched-exponential function with the following expression (Equation (6))

$$V_T(t) = V_0 \left\{ \exp \left[ - \left( \frac{t}{\tau} \right)^\beta \right] \right\} + c \quad (6)$$

The results of the fit for the two sets of measurements on P3HT are shown in **Figure 14**. Also in this case, the stretched exponential-based function is consistent in reproducing the experimental data, even if the adjusted  $R$ -square values resulted to be slightly lower than the previous ones (see **Table 4**). The most interesting aspect revealed from the model is the different values of the relaxation time  $\tau$  between the first and the second set. In particular,  $\tau$  resulted to be much greater during the first measurement rather than the second one, while the dispersion parameter is almost constant. As a consequence, during the second measurement, the stabilization of the threshold voltage was much faster and we attribute this effect to the rearrangement of the polymer chains due to the contact with water, as deducible from Raman characterizations (see Table S1 and Figure S5 in the Supporting Information). This result could be extremely important for the design of proper stabilization protocols for P3HT-based sensors, since the drift may be

**Table 4.** Fit parameters for the stretched exponential function of the first set and the combined (stretched exponential with square root dependence) function of the two sets of measurements of P3HT.

P3HT	Stretched exponential (1st set)	Stretched exponential (2nd set)
$V_0$ [mV]	-59	-57
$\tau$ [s]	3816	226
$\beta$	0.533	0.510
$c$ [mV]	-215	-242
Adj. $R$ -square	0.9906	0.9902

reduced in time, thanks to a precise electrical stress protocol prior the sensing measurements. This is another evidence of the differences in terms of stability between P3HT and P3CPT, since a prestress on the latter would not improve the stabilization, but would instead induce a worsening on the performance.

Finally, a discussion about the physical meaning of the stretched exponential behavior for the two polymers presented in this study must be addressed. As a matter of fact, this model was first developed to describe the instabilities in OFETs with solid insulating material and it was associated to the filling of trapping states caused by the EBS, as discussed above. For P3CPT, the charge trapping mechanism can be associated to an oxidative degradations enabled by the presence of the polar side chains.<sup>[34]</sup> This mechanism reduces the conduction in the polymer that is reflected on the increase of the absolute value of the threshold voltage.

However, for P3HT, the EBS applied through pulsed  $I_D$ - $V_G$  curves causes a reduction of the threshold voltage absolute value, which means that for the same value of the gate voltage, there are more charged carriers available. Thus, this shift of the threshold voltage should not be associated to trapping mechanism in this polymer. A possible explanation could be the presence of residual polarizations on the polymer that are induced by the EBS. In fact, it is known that P3HT is an electroactive material, i.e., its surface may change upon the application of a bias.<sup>[61]</sup> The slight modification of the surface may temporally trap negative ions in the topmost superficial layers of the polymer, which electrochemically dope the organic semiconductor for the next cycle. In fact, these ions contribute to the accumulation of holes in the P3HT, which causes the decrease of the threshold voltage absolute value as reported in the experimental data (i.e., the effective gate voltage to accumulate the same number of holes is lower in module). When the bias is removed from the system, the ions trapped on the surface are released into the electrolyte with a consequent increase of the absolute value of the threshold voltage and eventually restoring the initial values. Interestingly, the short-term behavior of P3HT is different depending on the kind of EBS applied: while

in the continuous bias stress mode, it was found a reduction of the EGOFT performance (lower transconductance and greater absolute values of the threshold voltage), in the pulsed mode, it was registered an opposite behavior. However, both these effects in the authors' opinion can be rationalized in terms of an interfacial electrochemical doping accompanied by the conformational reorganization of polymer backbones at the interface with the electrolyte. While, during pulsed measurement, a limited amount of anions may intercalate the topmost polymer layers, mainly contributing with an increase in charge carrier density, the prolonged application of a fixed bias could force a larger amount of ions to intercalate, therefore inducing a stronger conformational disorder and in turn reducing the overall charge transport properties.

This is a further proof that the two EBS modes stimulate differently the OSC/electrolyte interface with a dramatic impact on the EGOT stability.

## 4. Conclusion

EGOTs necessitate a deeper understanding about the causes of performance degradation and device instabilities. In this work, we investigated the effects of the electrical bias stress on EGOT fabricated with the organic semiconductors P3HT and P3CPT. Two different procedures were exploited for the bias application, namely the continuous and the pulsed electrical bias stress.

We found that the continuous EBS causes a worsening of the performance for both the polymers, with a more severe effect on P3CPT. The maximum drain current losses after 2 h of continuous EBS were 41% and 93% for P3HT and P3CPT, respectively. Nonresonant Raman characterizations allowed to ascribe the P3CPT performance degradation to an increase of conformational disorder due to the formation of polaronic species induced by the oxidation of the polymer to its quinoid form, enabled by the presence of the polar side chains. On the other hand, the minor deterioration of P3HT electronic performances is reflected in the absence of clear signs of oxidative degradation in its Raman spectra. Oxidation of P3HT side chains was observed only through XPS characterization. This result may be attributed to the hydrophobic nature of P3HT side chains, which may limit the intercalation of water molecules and of ions to the topmost interfacial molecular layers.

The pulsed EBS measurements allowed for real time monitoring of  $V_T$  and  $G_{max}$ . A reversible enhancement of P3HT performance was observed and could be attributed to an interfacial polarization taking place during each  $I_D-V_G$  cycle, thanks to the polymer electroactivity. P3CPT performance degradation could instead again be rationalized in terms of the oxidative degradation processes inferred by Raman and XPS spectroscopy.

Finally, a stretched exponential model commonly employed in the literature to describe EBS-induced charge trapping in solid insulating dielectric OFETs, was here exploited to fit liquid-dielectric EGOT experimental data from pulsed EBS measurements. The extracted relaxation time  $\tau$  and dispersion parameter  $\beta$  were consistent with values found in the literature for both polymers. In order to take into account the variation of the product  $\mu \cdot C$  in P3CPT-based device, a novel improvement to the stretched exponential model has been

proposed. An additional term with a square root dependency on time taking into account the polymer degradation enabled the accurate fitting of  $V_T$  over multiple  $I_D-V_G$  measurements sets interspersed with 1 h recovery pause. This effective term accounting for polymer degradation, together with the stretched exponential describing charge trapping mechanisms, allows for a more detailed description of EGOT electronic behavior under the influence of EBS.

## Supporting Information

Supporting Information is available from the Wiley Online Library or from the author.

## Acknowledgements

The present work was performed in the framework and financed by DEFLECT ("Advanced platform for the early detection of not small cells lung cancer") project, financed by the Piedmont Region in the framework of "Health & WellBeing" Platform project.

Open access Funding provided by Politecnico di Torino within the CRUI-CARE Agreement.

## Conflict of Interest

The authors declare no conflict of interest.

## Data Availability Statement

The data that support the findings of this study are available from the corresponding author upon reasonable request.

## Keywords

bias stress, EGOFTs, EGOTs, OECTs, organic electronics

Received: December 7, 2021

Revised: March 29, 2022

Published online:

- [1] M. Berto, C. Diacci, R. D'Agata, M. Pinti, E. Bianchini, M. Di Lauro, S. Casalini, A. Cossarizza, M. Berggren, D. Simon, G. Spoto, F. Biscarini, C. A. Bortolotti, *Adv. Biosyst.* **2018**, 2, 1700072.
- [2] M. Berto, S. Casalini, M. Di Lauro, S. L. Marasso, M. Cocuzza, D. Perrone, M. Pinti, A. Cossarizza, C. F. Pirri, D. T. Simon, M. Berggren, F. Zerbetto, C. A. Bortolotti, F. Biscarini, *Anal. Chem.* **2016**, 88, 12330.
- [3] V. Bertana, G. Scordo, M. Parmeggiani, L. Scaltrito, S. Ferrero, M. G. Gomez, M. Cocuzza, D. Vurro, P. D'Angelo, S. Iannotta, C. F. Pirri, S. L. Marasso, *Sci. Rep.* **2020**, 10, 13335.
- [4] L. Kergoat, B. Piro, M. Berggren, M. C. Pham, A. Yassar, G. Horowitz, *Org. Electron.* **2012**, 13, 1.
- [5] Y. Fu, N. Wang, A. Yang, Z. Xu, W. Zhang, H. Liu, H. K. W. Law, F. Yan, *Anal. Chem.* **2021**, 93, 14359.
- [6] M. Sensi, M. Berto, S. Gentile, M. Pinti, A. Conti, G. Pellacani, C. Salvarani, A. Cossarizza, C. A. Bortolotti, F. Biscarini, *Chem. Commun.* **2021**, 57, 367.



- [7] P. D'Angelo, G. Tarabella, A. Romeo, S. L. Marasso, M. Cocuzza, C. Peruzzi, D. Vurro, G. Carotenuto, S. Iannotta, *AIP Conf. Proc.* **2018**, 1990, 020015.
- [8] P. Cavassin, A. Pappa, C. Pitsalidis, H. F. P. Barbosa, R. Colucci, J. Saez, Y. Tuchman, A. Salleo, G. C. Faria, R. M. Owens, *Adv. Mater. Technol.* **2020**, 5, 1900680.
- [9] M. Nikolka, *MRS Commun.* **2020**, 10, 98.
- [10] M. Parmeggiani, A. Verna, A. Ballesio, M. Cocuzza, E. Piatti, V. Fra, C. F. Pirri, S. L. Marasso, *Sensors* **2019**, 19, 4497.
- [11] S. Inal, G. G. Malliaras, J. Rivnay, *Nat. Commun.* **2017**, 8, 1767.
- [12] A. Sharma, S. G. J. Mathijssen, M. Kemerink, D. M. de Leeuw, P. A. Bobbert, *Appl. Phys. Lett.* **2009**, 95, 253305.
- [13] P. A. Bobbert, A. Sharma, S. G. J. Mathijssen, M. Kemerink, D. M. de Leeuw, *Adv. Mater.* **2012**, 24, 1146.
- [14] T. Cramer, A. Campana, F. Leonardi, S. Casalini, A. Kyndiah, M. Murgia, F. Biscarini, *J. Mater. Chem. B* **2013**, 1, 3728.
- [15] D. Blasi, F. Viola, F. Modena, A. Luukkonen, E. Macchia, R. A. Picca, Z. Gounani, A. Tewari, R. Österbacka, M. Caironi, Z. M. Kovacs Vajna, G. Scamarcio, F. Torricelli, L. Torsi, *J. Mater. Chem. C* **2020**, 8, 15312.
- [16] R. A. Picca, K. Manoli, E. Macchia, A. Tricase, C. Di Franco, G. Scamarcio, N. Cioffi, L. Torsi, *Front. Chem.* **2019**, 7, 667.
- [17] A. Luukkonen, *Characterisation and Modelling of Stability Issues in EGFET Devices* **2020**.
- [18] S.-M. Kim, C.-H. Kim, Y. Kim, N. Kim, W.-J. Lee, E.-H. Lee, D. Kim, S. Park, K. Lee, J. Rivnay, M.-H. Yoon, *Nat. Commun.* **2018**, 9, 1.
- [19] K. Asano, P. Didier, K. Ohshiro, N. Lobato-Dauzier, A. J. Genot, T. Minamiki, T. Fujii, T. Minami, *Langmuir* **2021**, 37, 7305.
- [20] A. Tibaldi, L. Fillaud, G. Anquetin, M. Woytasik, S. Zrig, B. Piro, G. Mattana, V. Noël, *Electrochim. Commun.* **2019**, 98, 43.
- [21] H. Toss, C. Suspène, B. Piro, A. Yassar, X. Crispin, L. Kergoat, M. C. Pham, M. Berggren, *Org. Electron.* **2014**, 15, 2420.
- [22] B. V. Khau, L. R. Savagian, M. De Keersmaecker, M. A. Gonzalez, E. Reichmanis, *ACS Mater. Lett.* **2019**, 1, 599.
- [23] H. Sun, M. Vagin, S. Wang, X. Crispin, R. Forchheimer, M. Berggren, S. Fabiano, *Adv. Mater.* **2018**, 30, 1704916.
- [24] M. Segantini, M. Parmeggiani, A. Ballesio, G. Palmara, F. Frascella, S. L. Marasso, M. Cocuzza, *Sensors* **2022**, 22, 969.
- [25] R. G. Bates, J. B. Macaskill, *Pure Appl. Chem.* **1978**, 50, 1701.
- [26] S. Trasatti, *J. Electroanal. Chem.* **1986**, 209, 417.
- [27] K. Bruchlos, D. Trefz, A. Hamidi-Sakr, M. Brinkmann, J. Heinze, A. Ruff, S. Ludwigs, *Electrochim. Acta* **2018**, 269, 299.
- [28] A. Laiho, L. Herlogsson, R. Forchheimer, X. Crispin, M. Berggren, *Proc. Natl. Acad. Sci. USA* **2011**, 108, 15069.
- [29] P. D'Angelo, S. L. Marasso, A. Verna, A. Ballesio, M. Parmeggiani, A. Sanginario, G. Tarabella, D. Demarchi, C. F. Pirri, M. Cocuzza, S. Iannotta, *Small* **2019**, 15, 1902332.
- [30] P. D'Angelo, N. Coppedè, G. Tarabella, A. Romeo, F. Gentile, S. Iannotta, E. Di Fabrizio, R. Mosca, *Org. Electron.* **2014**, 15, 3016.
- [31] M. G. Jeong, H. O. Seo, D. H. Kim, K. D. Kim, E. J. Park, Y. D. Kim, D. C. Lim, *J. Phys. Chem. C* **2014**, 118, 3483.
- [32] Q. Zhang, A. Tamayo, F. Leonardi, M. Mas-Torrent, *ACS Appl. Mater. Interfaces* **2021**, 13, 30902.
- [33] M. Chandra, *Buffer: A Guide for the Preparation and use of Buffers in Biological Systems*, EMD Biosciences, Inc., Merck KGaA, Darmstadt, Germany **2006**.
- [34] T. Minamiki, Y. Hashima, Y. Sasaki, T. Minami, *Chem. Commun.* **2018**, 54, 6907.
- [35] G. Shi, J. Xu, M. Fu, *J. Phys. Chem. B* **2002**, 106, 288.
- [36] G. Louarn, M. Trznadel, J. P. Buisson, J. Laska, A. Pron, M. Lapkowski, S. Lefrant, *J. Phys. Chem.* **1996**, 100, 12532.
- [37] S. Bellani, D. Fazzi, P. Bruno, E. Giussani, E. V. Canesi, G. Lanzani, M. R. Antognazza, *J. Phys. Chem. C* **2014**, 118, 6291.
- [38] H. Peng, L. Zhang, J. Spires, C. Soeller, J. Travas-Sejdic, *Polymer* **2007**, 48, 3413.
- [39] M. Baibarac, M. Lapkowski, A. Pron, S. Lefrant, I. Baltog, *J. Raman Spectrosc.* **1998**, 29, 825.
- [40] G. M. Paternò, V. Robbiano, K. J. Fraser, C. Frost, V. García Sakai, F. Cacialli, *Sci. Rep.* **2017**, 7, 1.
- [41] Y. Gao, J. K. Grey, *J. Am. Chem. Soc.* **2009**, 131, 9654.
- [42] W. C. Tsoi, D. T. James, J. S. Kim, P. G. Nicholson, C. E. Murphy, D. D. C. Bradley, J. Nelson, J. S. Kim, *J. Am. Chem. Soc.* **2011**, 133, 9834.
- [43] F. L. Galeener, J. C. Mikkelsen, *Solid State Commun.* **1981**, 37, 719.
- [44] J. Yamamoto, Y. Furukawa, *J. Phys. Chem. B* **2015**, 119, 4788.
- [45] M. Trznadel, M. Zagórska, M. Lapkowski, G. Louarn, S. Lefrant, A. Pron, *J. Chem. Soc., Faraday Trans.* **1996**, 92, 1387.
- [46] S. Ludwigs, in *P3HT Revisited – From Molecular Scale to Solar Cell Devices*, Springer, Berlin **2014**, pp. 39–82.
- [47] T. Schwieger, X. Liu, H. Peisert, B. Adolph, N. Kiri, M. Knupfer, *J. Appl. Phys.* **2005**, 97, 123712.
- [48] D. H. Kim, M. G. Jeong, H. O. Seo, Y. D. Kim, *Phys. Chem. Chem. Phys.* **2015**, 17, 599.
- [49] B. P. Silva Santos, J. J. Rubio Arias, L. S. Albuquerque, A. G. da Veiga, J. G. de Melo Furtado, A. de Castro Ribeiro, L. A. F. da Silva, E. V. Bendinelli, M. L. M. Rocco, R. Valaski, M. de Fatima, V. Marques, *J. Electron Spectrosc. Relat. Phenom.* **2019**, 234, 27.
- [50] M. Manceau, J. Gaume, A. Rivaton, J. L. Gardette, G. Monier, L. Bideux, *Thin Solid Films* **2010**, 518, 7113.
- [51] M. Manceau, A. Rivaton, J. L. Gardette, S. Guillerez, N. Lemaître, *Polym. Degrad. Stab.* **2009**, 94, 898.
- [52] S. W. Han, S. W. Joo, T. H. Ha, Y. Kim, K. Kirn, *J. Phys. Chem. B* **2000**, 104, 11987.
- [53] S. Stepanow, T. Strunskus, M. Lingenfelder, A. Dmitriev, H. Spillmann, N. Lin, J. V. Barth, C. Wöll, K. Kern, *J. Phys. Chem. B* **2004**, 108, 19392.
- [54] A. Sharma, S. G. J. Mathijssen, E. C. P. Smits, M. Kemerink, D. M. De Leeuw, P. A. Bobbert, *Phys. Rev. B. Phys.* **2010**, 82, 075322.
- [55] H. Sinno, S. Fabiano, X. Crispin, M. Berggren, I. Engquist, *Appl. Phys. Lett.* **2013**, 102, 113306.
- [56] H. Lee, B. Moon, S. Y. Son, T. Park, B. Kang, K. Cho, *ACS Appl. Mater. Interfaces* **2021**, 13, 16722.
- [57] B. Kang, B. Moon, H. H. Choi, E. Song, K. Cho, *Adv. Electron. Mater.* **2016**, 2, 1500380.
- [58] W. H. Lee, H. H. Choi, D. H. Kim, K. Cho, *Adv. Mater.* **2014**, 26, 1660.
- [59] S. G. J. Mathijssen, M. Cölle, H. Gomes, E. C. P. Smits, B. de Boer, I. McCulloch, P. A. Bobbert, D. M. de Leeuw, *Adv. Mater.* **2007**, 19, 2785.
- [60] L. Torsi, M. Magliulo, K. Manoli, G. Palazzo, *Chem. Soc. Rev.* **2013**, 42, 8612.
- [61] S. Liu, Y. Fu, G. Li, L. Li, H. K.-w. Law, X. Chen, F. Yan, *Adv. Mater.* **2017**, 29, 1701733.